Nonlinear optical studies of single gold nanoparticles

Dijk, M.A. van

Citation

Dijk, M. A. van. (2007, October 17). *Nonlinear optical studies of single gold nanoparticles*. *Casimir PhD Series*. Retrieved from https://hdl.handle.net/1887/12380

5

Correlation of optical and structural properties

5.1 Introduction

The optical responses of gold nanoparticles as studied in this thesis carry signatures of their structural properties, such as their size and shape, and also of their environment. For example, the period of the acoustic vibration depends strongly on the size of the particle and is hardly affected by anything else, while the damping time on the other hand is strongly influenced by the elastic coupling of the particle to its close environment (see chapter 1 and [50]). Like snowflakes, no two gold nanoparticles are exactly alike. Electron microscopy images show a rich variety in sizes and shapes within a sample of particles of nominally the same size. The ultimate goal of this chapter is to try to make a correlation between the optical effects that we detect and the structure of the individual particles. Obviously this is a rather ambitious objective, since the structural properties manifest themselves only indirectly. The spatial resolution of optical experiments is limited to the wavelength of the light source, which in our case exceeds the dimensions of the particles by far. Electron microscopy, exploiting the much shorter wavelength of electrons, can achieve a much higher resolution, up to the atomic scale, and is therefore capable of accurately mapping the structure of the particle. Ideally, we should therefore combine our optical experiments with electron microscopy on the exact same particle. Although these experiments, that are far from trivial, are currently pursued in our lab, here we will still have to do without.

Besides electron microscopy, there are a number of other methods that can be used to acquire more information about the structure of a nanoparticle. One of those methods is white-light spectroscopy, a method with which the absorption spectrum of a particle can be measured. Polarization dependent measurements of the absorption spectrum can give information on the ellipticity and orientation of the particle [106]. Additionally we can obtain structural information from time-resolved experiments. A measurement of the period of the acoustic vibration can for example yield the size of the particle, although assumptions about the shape and environment of the particle have to be included in the calculation [50, 48]. Another method to correlate optical and structural properties is statistical analysis of many single particles. By comparing electronic and vibrational properties of many individual particles, not only can we gain insight into the average properties of the ensemble, but we can also investigate the differences between particles by plotting histograms of several parameters. By doing experiments on single particles, it is for the first time possible to directly measure the homogeneous damping of the particles, which is solely governed by the elastic interaction of the particle and its local environment.

In the first part of this chapter, we explain the white-light spectroscopy experiments and show that it is possible to make a first-order determination of the shape of our particles. We then proceed to combine white-light spectroscopy and pump-probe interferometry on the same particle, in order to unravel the processes behind the signals that are detected in the pump-probe experiments. The second part contains a statistical analysis of the electronic and vibrational properties of a large collection of single particles. We will also make a first step towards investigating the effect of the environment on the period and damping time of the acoustic vibrations by studying gold nanoparticles that are coated with a layer of silica. Finally, in section 5.4, we present some more detailed experiments on particles that show a second vibrational mode, associated with ellipsoidal deformation, that were already touched upon in section 4.5.

5.2 Combination of white-light spectroscopy and pump-probe interferometry

We show the combination of white-light spectroscopy, with which the absorption spectra of single gold nanoparticles can be measured, and the pump-probe technique that has been presented in chapters 3 and 4. In this experiment, light is reflected from a surface on which gold nanoparticles are deposited. The reflected light is collected on a spectrometer, and contains contributions from light that is scattered by the particle and light that is reflected from the interface. From the interference of these two contributions, the scattering and absorption spectra can be extracted.

5.2.1 Experimental method

White light from a high-power gas discharge lamp is focussed with an air-spaced objective (Olympus, 60×, NA = 0.9, cover-slide corrected) on an interface between microscopy immersion oil and a cover slide on which gold nanoparticles are spincoated. The samples were prepared using the method described in section 3.2. The reflected light that is collected, is a superposition of the waves that are reflected from the interface and of the waves that are scattered by the particles. We can detect the reflected light with a photon-counting APD (PerkinElmer) or with a spectrometer (SpectroPro 500i, Acton Research) and a liquid-nitrogen-cooled CCD-camera (Spec-10, Princeton Instruments). A bandpass filter, transmitting light between 450 and 700 nm was placed before the APD. In order to select a proper beam profile, a pinhole of 15 μm diameter was placed in the focus of the beam expander in the excitation path. A sketch of the white-light scattering setup is shown in Fig. 5.1A, while a typical source spectrum of the Xenon lamp is plotted in Fig. 5.1B. The pump-probe experiment is explained in detail in chapter 3.

If an incident field E_i is focused onto an interface, the reflected field is $E_r = rE_i e^{-i\pi/2}$ (with r the reflection coefficient of the interface, and a phase of $\pi/2$ has been introduced to account for the Gouy phase shift [66]). Following [66] further, the field scattered from the particle is $E_s = s(\lambda)E_i$, where $s = |s(\lambda)|e^{\phi(\lambda)}$ is given by

$$s = \eta\alpha(\lambda), \tag{5.1}$$

where η is a factor describing the geometry of the experiment with the particle in the focal spot, with dimension $1/V$. $\alpha(\lambda)$ is the polarizability of the particle (Eq. (1.15)). The intensity I_{det} measured at the detector is a superposition of the light that is reflected from the interface and the light that is scattered by the particle.

$$I_{det} = |E_r + E_s|^2 = |E_i|^2 \left(r^2 + |s|^2 - 2r|s|\sin(\phi)\right) \tag{5.2}$$

To measure the spectrum of the particle $\sigma(\lambda)$, we have normalized the spectrum recorded with a particle in the focus $I_{det}(\lambda)$ to a signal recorded next to

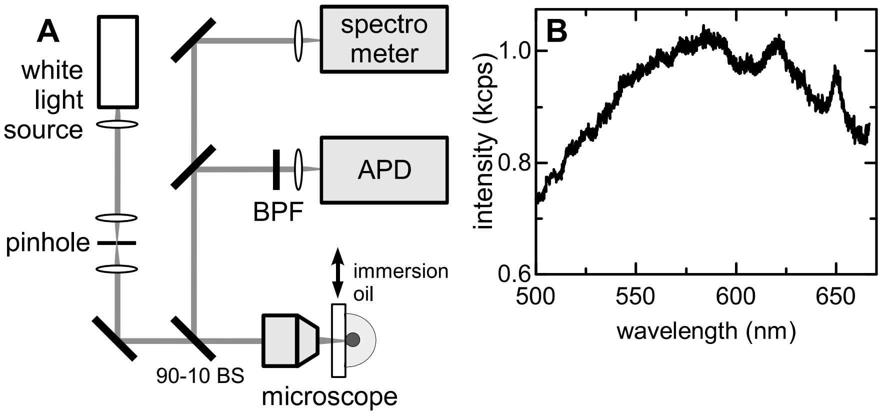

Figure 5.1: (A) Schematic drawing of the setup used for white-light spectroscopy of single gold nanoparticles. Light from a Xenon lamp is reflected from an interface on which gold nanoparticles are dispersed. From the interference of the reflected light and the light scattered by the particle, collected by a spectrometer, the absorption spectra can be deduced. With the APD, confocal scans of the sample can be made. The 90-10 BS is a beam splitter that reflects 90% of the light and transmits 10%. The BPF is a band-pass filter that transmits light between 450 and 700 nm. (B) Typical spectrum of the white-light source.

the particle $I_r(\lambda)$ (typically 3 μm away):

$$\begin{aligned}\sigma(\lambda) = \frac{I_{det}(\lambda) - I_r(\lambda)}{I_r(\lambda)} &= \frac{\eta^2}{r^2}|\alpha(\lambda)|^2 - 2\frac{\eta}{r}|\alpha(\lambda)|\sin(\phi) \\ &= \frac{\eta^2}{r^2}|\alpha(\lambda)|^2 - 2\frac{\eta}{r}\mathrm{Im}\left[\alpha(\lambda)\right]\end{aligned} \tag{5.3}$$

We see that part of the signal has contributions proportional to $|\alpha(\lambda)|^2$ and to Im $[\alpha(\lambda)]$, similar to scattering (Eq. 1.17) and absorption spectra (Eq. 1.16), respectively. Note that the spatial dependence of the scattered and reflected fields are not equal. The reflected wave is a Gaussian wave, while the scattered wave is spherical. However, we neglect this inequality here, assuming that the NA of the reflected field is very large, so that it approximately overlaps with the scattered field.

5.2.2 White-light scattering

Figure 5.2A shows a confocal scan of 20 × 20 μm, of a sample containing gold nanoparticles with a nominal diameter of 60 nm, illuminated with unpolarized white light from a Xenon lamp. The light is detected by the APD through

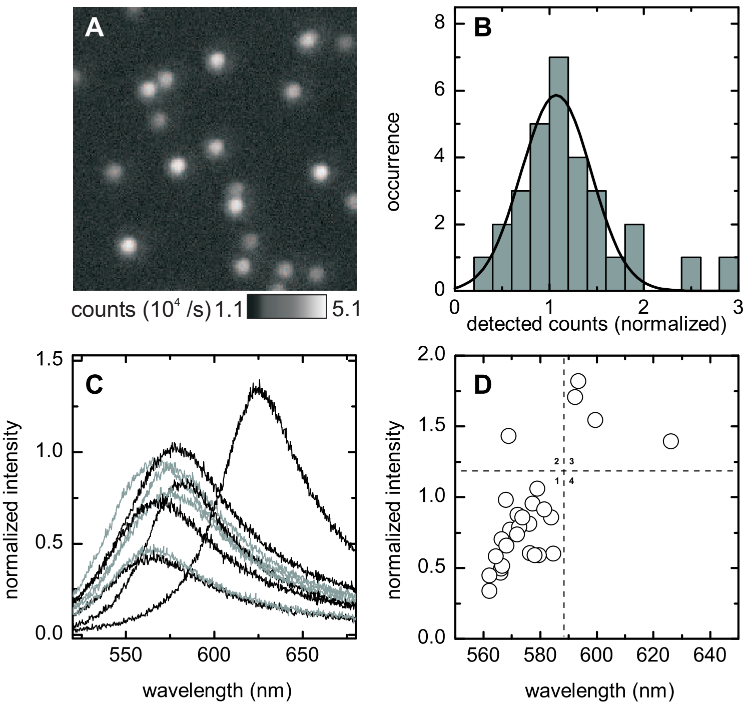

Figure 5.2: Scattering spectra with unpolarized white light from a high power Xenon gas discharge lamp, of gold nanoparticles with a nominal diameter of 60 nm, on a BK7 substrate in immersion oil. (A) 20x20 μm image of light collected on the APD while scanning the sample through the focus of the microscope. (B) Histogram of normalized scattered intensities as collected with the APD. The intensities were normailzed as $I_{norm} = (I_{peak} - I_{bg})/I_{bg}$. The solid line is a Gaussian fit of the histogram, yielding a width of 37%. (C) Spectra recorded for the spots in (A) in the focus of the microscope, normalized to a background spectrum next to the particle. (D) Maximal normalized intensity of 28 spectra, including those shown in (C), plotted against the wavelength of the maximum. The four quadrants are used to classify the particles as single or double particles, see text for details.

a bandpass filter that transmits light between 450 nm and 700 nm. The particles are clearly detected, and a histogram of detected intensities, normalized to the background here, of 28 particles (see Fig. 5.2B) shows a monomodal distribution, of which the relative width is about twice the volume distribution as it is specified by the manufacturer, indicating that we detect single particles here. The spots in this image have a width of about 1 μm (FWHM) and a signal-to-noise ratio of roughly 30.

Figure 5.2C shows spectra of the particles in Fig. 5.2A, again measured with unpolarized light and normalized to a background spectrum, measured roughly 3 μm away from each particle. Most of the spectra have a peak between 560 and 580 nm, however, one of the spectra is largely red shifted compared to the others. The distribution of maximum detected intensities is comparable to the distribution shown in Fig. 5.2A, with the red shifted particle also here as an outlier. The peak wavelength is plotted against the maximum intensity in Fig. 5.2D, for the spectra shown in Fig. 5.2C and 18 other spectra. To make a distinction between the different types of spectra, we have divided this plot in four quadrants. Most spectra fall in the first quadrant, with peak wavelengths below 590 nm and a maximum normalized intensity below 1.2. The intensity distribution in these spectra resembles the Gaussian distribution in the histogram of Fig. 5.2B, and these spectra stem from single particles. The outliers of the distribution either lie in quadrant 2, having a high maximum intensity, but a peak wavelength below 590 nm, or in quadrant 3, having a high maximum intensity and a highly red-shifted peak wavelength. These latter spectra most likely stem from close pairs of particles. The spectrum in quadrant 2 is simply the sum of two single-particle spectra, located far away from each other so that there is no interaction. The red shift of the spectra in quadrant 3 can be explained by a near-field interaction of the electrons of two particles located close together. The longitudinal plasmon that is thus created gives rise to a largely red-shifted spectrum. No particles are located in the fourth quadrant. A particle that would fall in this square could for example be a rod-shaped particle with roughly the same volume as a sphere with a 60-nm diameter. Although electron microscopy shows that such shapes can occur in our samples, no such particles have been detected here.

The elongation and orientation of the particles in the plane of the sample can be determined from spectra measured with polarized white light [106]. If a particle is elongated, a second, red-shifted, peak appears in the spectrum, which is associated with a plasmon polarized along the long axis of the elongated particle. The intensity of the longitudinal peak strongly depends on polarization. If the elongation is small, the two modes fall close together and cannot be distinguished. The spectrum of a slightly elongated particle therefore appears as a single peak, which red-shifts as the polarization of the source is rotated. A major drawback of this method is that it is completely blind for elongations perpendicular to the sample plane. A previous study that used polarization dependent absorption spectra to determine the shape and orientation of nanoparticles used the dipole approximation to model the spectra [106]. Our particles are too large for this approximation and we have

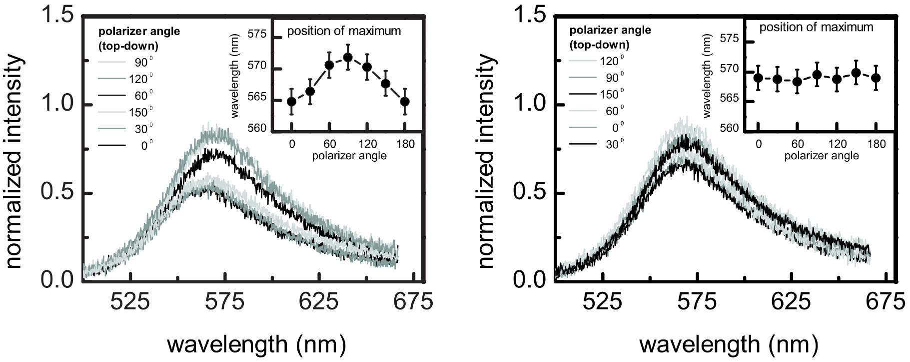

Figure 5.3: Scattering spectra using linearly polarized white light, as functions of polarization angle, of 30-nm radius particles in immersion oil, on a sample of BK7 glass. In (A) the spectra shift as the polarization angle is rotated, which means that the particle is elongated. In (B), the spectra are independent of polarization angle, indicating that the particle is possibly spherical.

to use Mie theory, which only applies to spherical particles. To determine the absorption spectra of large non-spherical particles, numerical methods such as the T-matrix method [107, 108] have to be used. Since at this point, we are only qualitatively interested in the question whether the particles are spherical or not, and not quantitatively in their ellipticity, we have not attempted to model the polarization dependence of these spectra. To obtain an idea of the order of magnitude of the detected elongations, in the dipole approximation, a red shift of 5 nm for perpendicular polarizations, as observed in Fig. 5.3A, gives an aspect ratio (short axis of the particle divided by the long axis of the particle) of 0.9 [106].

Figure 5.3 shows spectra of two single gold nanoparticles, as functions of the polarization direction of the light source. In Fig. 5.3A, the spectrum red shifts as the polarization changes, with a 90° difference between the minimum and maximum red shift. This particle is clearly elongated. For the particle in Fig. 5.3B, there is no red shift observed at all as the polarization is rotated. For this particle we can conclude that, at least in the sample plane, it is spatially isotropic. Although there is no red shift detected for this particle, there is a significant change in the normalized intensity of the spectrum as the polarization is rotated. The maximum intensity is detected at 120 degrees, and in fact, all polarization-dependent spectra have a bias towards this value, even spectra of particles that have the maximum red shift away from 120°. We therefore do not believe that this effect is caused by the particle, but rather that it is an artefact of the measurement, most probably an imperfection in the normalization, possibly caused by a mismatch between the Gaussian wave of the source and the spherical scattered wave. Note that the 120 degrees is measured in the frame of the polarizer, and corresponds to an angle of 45 degrees from vertical in the laboratory frame.

5.2.3 White-light and pump-probe spectra of the same particle

By combining white-light spectroscopy with pump-probe interferometry, we can now correlate the ultrafast properties of the particle measured in the pump-probe experiment directly with the absorption spectrum that we know from the white-light experiment. In this way, we hope to exclude shape effects from the measurements by selecting spherical particles, and moreover we can gain a better insight into the mechanisms behind our detection scheme. In order to do so, we first have to extract the absorption spectrum from the spectra that we measure.

From the similarity of Eq. (5.3) to contributions from scattering and absorption, we have chosen to fit our spectra with a linear combination of absorption and scattering spectra Eqs. (1.4) and (1.5).

$$\sigma(\lambda, R) = A(R, \eta) \left[\sigma_{sca}(\lambda, R) - B(R)\sigma_{abs}(\lambda, R)\right] + C \tag{5.4}$$

With a known dielectric function of the particle [27], and assuming that the particles are spherical, the Mie spectra only depend on the radius of the particle and the refractive index of the environment. These two parameters cannot be determined independently, thus we have to fix one. In the configuration that we have chosen here, with the particles embedded in immersion oil, the refractive index is well defined, and therefore fixed at 1.52. We now find a radius of the particle from our fit and using this, we can reconstruct the absorption spectrum of the particle. Note that the fit function above assumes that the particles are completely spherical, and that the radius that is returned is only valid for the chosen refractive index of the medium, while we cannot exclude local variations of the index of refraction. We therefore only use this fit to determine the absorption spectrum, and not to find structural parameters such as the radius of the particle.

For four different particles, we have determined the absorption spectra in this way, and we have combined this with pump-probe measurements with six different probe wavelengths between 523 and 609 nm. Figure 5.4 shows these delay traces for one particle. We see that the electronic amplitude, defined as the magnitude of the first peak in the delay scans, changes sign between 550 nm and 570 nm, and that the phase of the vibrations makes a 180°

phase shift between 530 nm and 550 nm. Also at 550 nm, the electronic amplitude is strongest, while the vibrations are weakest. We have determined the intensity of the electronic amplitude and the amplitude of the oscillations for this and three other particles and compared these signals to absorption spectra measured with an unpolarized light source. This is shown for each particle separately in Fig. 5.5. The differential spectra, as measured in the pump-probe experiments, are completely different for the electronic signal and the acoustic vibration, due to their distinct spectral origin (see section 1.3.3). If we compare the differential spectra to the absorption spectra, we see that each particle shows a similar trend. The electronic signal peaks at the resonance, where the vibrations vanish. The maximum amplitude of the vibrations lies roughly halfway between the resonance and the half-width at half maximum in the red wing of the spectrum. In the blue wing, the vibrations are always much weaker than in the red wing. The polarization-dependence of the resonance wavelength is plotted for al four particles in Fig. 5.6.

To enable a more quantitative comparison between the differential and the absorption spectra, we have scaled all spectra according to

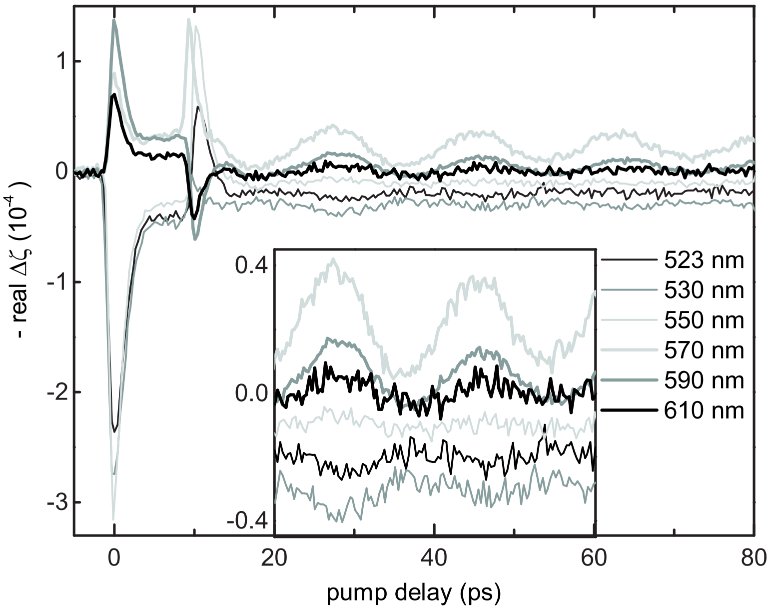

Figure 5.4: Delay traces of a single gold nanoparticle for six different probe wavelengths. The inset shows an enlarged crop of the oscillatory part of the traces. The pump power was kept constant at 125 μW in the sample plane.

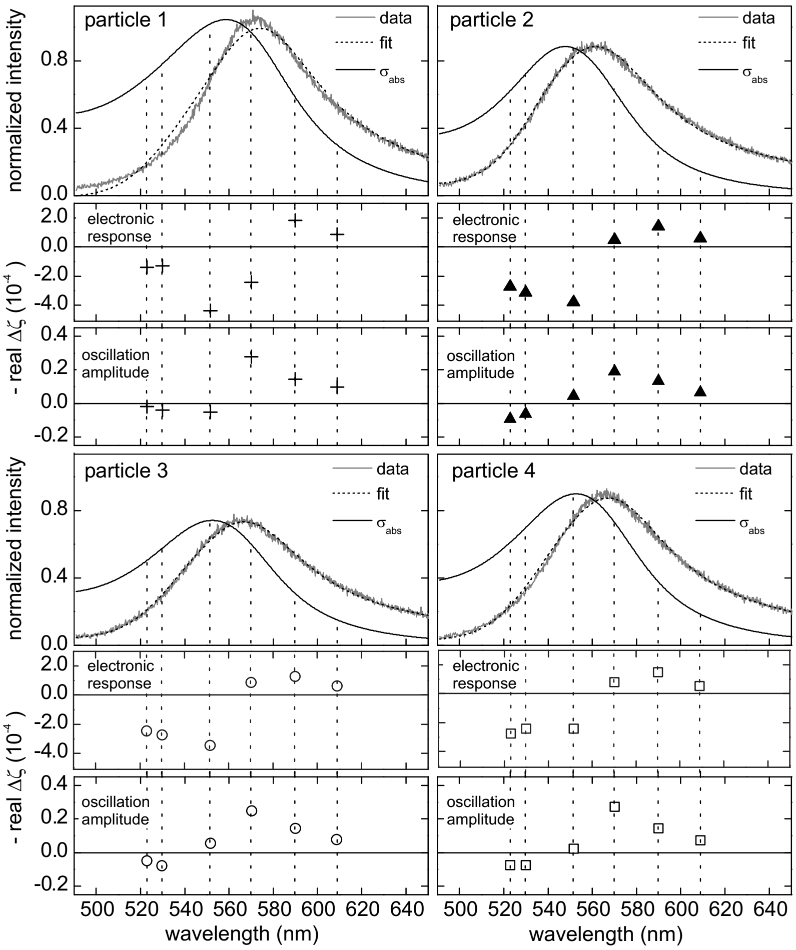

Figure 5.5: Comparison of absorption and pump-probe spectra of four different single gold nanoparticles. For each particle, the top panel shows white-light spectra as measured using an unpolarized source. The dotted lines are fits of the spectra to Eq. 5.4. The solid lines are plots of the corresponding absorption spectra. In the middle panel, the electronic response, defined as the highest point of the first peak in the delay traces, has been plotted for the corresponding probe wavelength. In the bottom panel, the oscillation amplitude has been plotted against the probe wavelength.

$$\lambda_s = \frac{\lambda - \lambda_0}{w} \tag{5.5}$$

where λ_0 is the resonance wavelength and w is the half width at half maximum in the red wing of the resonance. By applying this scaling, and normalizing all spectra, the absorption spectra almost fully overlap. The result of this transformation can be seen in Fig. 5.7, in the top panel for the absorption spectra and in the lower two panels for the electronic response and the acoustic vibrations. It appears that all points fall on the same curve. We have tried to model these results, using a model based on separation of the dielectric functions of the bound and free electrons, using a Drude model [26]. Heating of electrons and lattice were then calculated through their effect on the free electrons only. Although the rough behavior fits the experimental observations, the model was too simple to make accurate predictions. The effect of the bound electrons has to be included for a correct prediction of the differential spectra. The qualitative behavior however agrees with the optical contrast mechanisms explained in section 1.3.3.

To summarize these results, we have been able to measure white-light scattering spectra of single gold nanoparticles, and have correlated these spectra with pump-probe interferometry on the same particle. The results we find can be qualitatively explained by broadening as the contrast mechanism of the electronic peak, and with a periodic red shift of the surface plasmon resonance as the contrast mechanism of the acoustic vibrations. A quantitative theoretical explanation could unfortunately not be given. A model that only included excitation of the free electrons proved to be too simple to fully explain the experimental results.

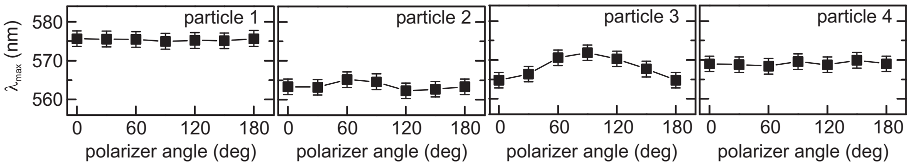

Figure 5.6: Wavelength of the resonance in the detected white-light spectra as a function of polarization angle of a polarized white-light source. These plots are a measure for the ellipticity of the particles.

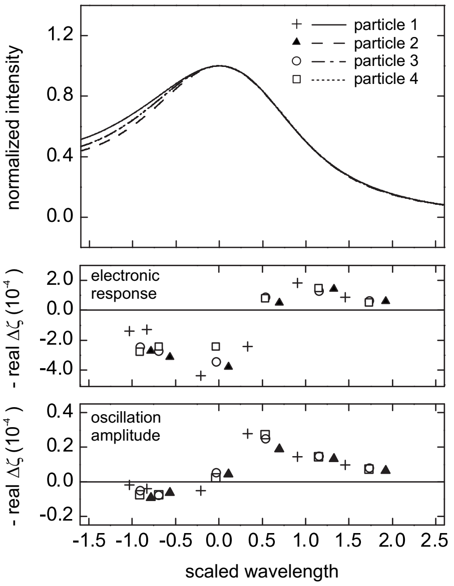

Figure 5.7: (A) Normalized absorption spectra of the 4 particles on a rescaled wavelength axis, where now all spectra fall one the same curve. The wavelength axis has been rescaled according to Eq. (5.5). (B) Electronic response for four different particles plotted against the rescaled wavelength. (C) Oscillation amplitude for four different particles plotted against the rescaled wavelength.

5.3 Statistical analysis of single-particle pump-probe dynamics

In order to gain more insight in the distribution of electronic and vibrational parameters of single gold particles within a sample, we have measured delay traces of many different particles under the same conditions, and have constructed histograms for the relevant parameters. Also shown here are first experiments on single gold nanoparticles coated with a layer of silica. For all experiments in this section, the probe wavelength was 590 nm. The sample preparation procedures were the same as explained in chapter 3.2. The BK7 substrates were cleaned with the procedure explained in chapter 3.2, the fused silica substrates were only ozone cleaned and did not undergo the KOH/acetone procedure.

We have measured delay traces of of 55 single gold nanoparticles with a nominal size of 60 nm, spincoated on BK7 glass. From the delay traces, we have determined the electronic amplitude by measuring the maximum

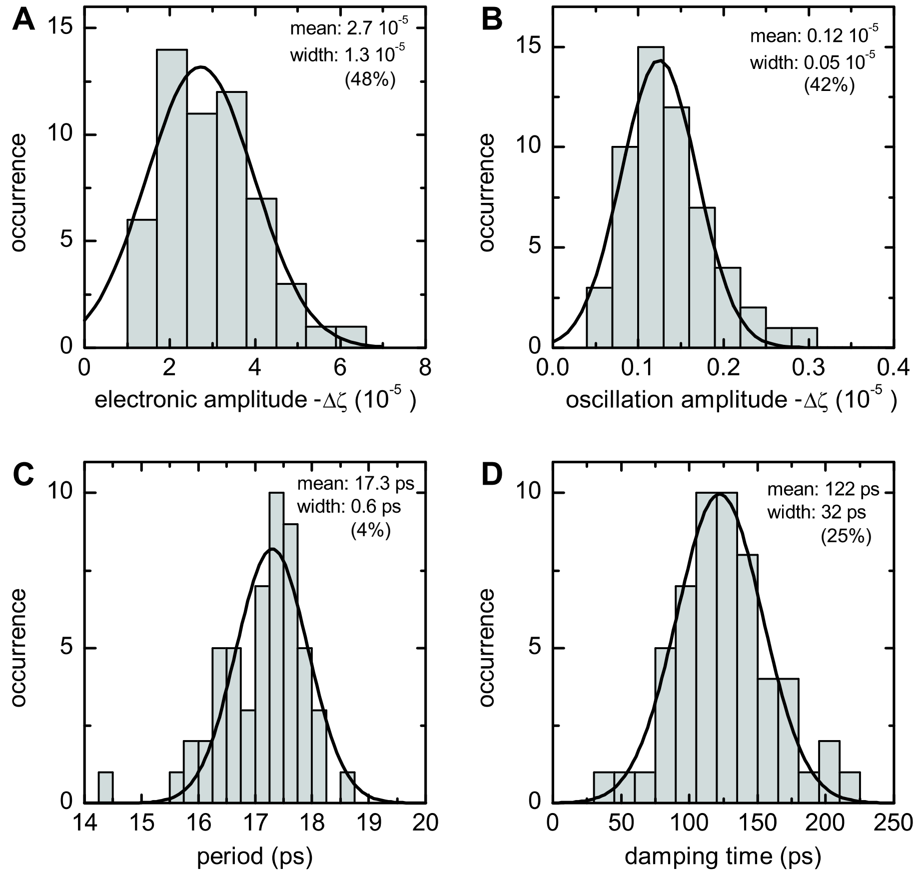

Figure 5.8: Histograms of fitted parameters of single-particle delay traces. Of 55 single particles, delay traces were measured under the same experimental conditions. Shown here are the magnitude of the first peak (electronic amplitude) (A), and the oscillation amplitude (B), period (C) and damping time (D). The particles have a nominal diameter of 60 nm, and were spincoated in a PVA solution on a cover slide of BK7 glass. All histograms could be fitted to a Gaussian distribution.

value of the first peak in the trace. The oscillation amplitude, period and damping time have been determined by fitting a damped cosine function to the oscillatory part of the trace. These parameters are plotted in histograms in Fig. 5.8. All histograms could be fitted to a Gaussian distribution.

The electronic amplitude (Fig. 5.8A) is expected to scale with the volume of the particle, since the detection method is based on absorption (see section 1.2). If the particles are assumed to be spherical and the environment

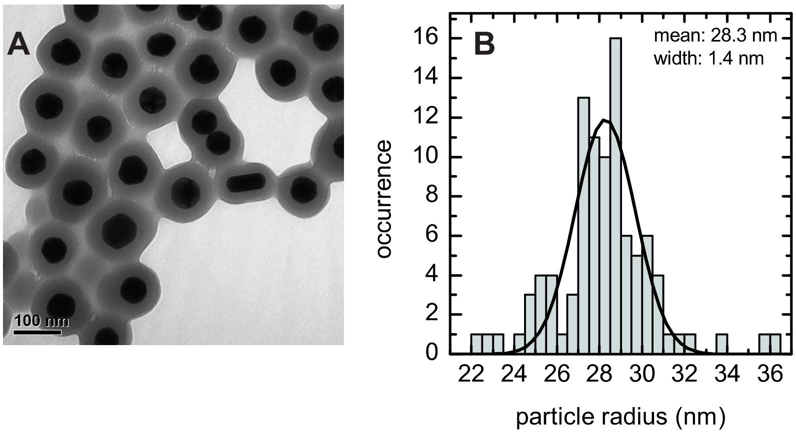

Figure 5.9: (A) TEM image of a sample of 60-nm gold nanoparticles coated with a 30-nm layer of silica (image by Peter Zijlstra). (B) Histogram of particle radii as determined from TEM images, assuming that the particles are spherical (the average circularity was 0.9, but this is neglected here). The mean radius is 28.3 nm, which does not correspond to the manufacturer's value of 30.1 nm. The width of the size distribution of the sample is 5%.

homogeneous, the width of this distribution should be 15%, three times the size distribution of the particles. The measured width of 50% is, however, much broader. There are a number of reasons for this. First of all, the method by which the peak value is determined is based on only one data point per delay trace, and is therefore prone to noise. Secondly, the particles are not spherical and the environment is not homogeneous, and these variations are amplified by the detection method. We measure a nonlinear effect, with the probe wavelength tuned to the most sensitive part of the spectrum, where $d\sigma/d\lambda$ is largest. As a result of this, small spectral variations are amplified, and broaden the distribution. The same holds for the oscillation amplitude (Fig. 5.8B), even though the spectral origin of this signal is different, as a result of which, the width of this distribution does not *a priori* have to be the same as that of the electronic response, even though here it is.

The histogram of vibration periods (Fig. 5.8C) is rather narrow, and with 4% very close to the size distribution as given by the manufacturer, which fits expectations, since the vibration period scales linearly with the size of the particle [17]. From the mean period, the average radius of the particles can be determined. Analysis of TEM images (Fig. 5.9, of particles from the same batch but coated with a 30-nm layer of silica, and assuming that the particles are spherical) yielded an average radius of 28.3 nm and a size distribution of

5%. Calculated vibration periods and damping times for a gold nanoparticle with a radius of 28 nm are given in Table 1.2 on page 30. From our experimental conditions, we would expect the vibration period to lie somewhere between the period of a gold nanoparticle fully embedded in glass and of the period of a free sphere (the period of a particle embedded in PVA falls in between these two values). The vibrational periods belonging to a 28.3 nm particle under those circumstances are 17.5 ps (embedded) and 18.6 ps (free). Our detected average value of 17.3 ps falls outside this range and is shorter than expected. The reason for this deviation is not clear, but may be related to the shape of the particles, since TEM analysis yielded an average circularity of 0.9. Another explanation could be that the sound velocities inside nanoparticles differ from bulk values.

The damping times that are collected in the histogram in Fig. 5.8D are homogeneous damping times. These can be directly studied for the first time, since the single-particle experiments are not hampered by inhomogeneous broadening, inevitable for ensemble measurements. We find a mean damping time of 122 ps, with a width of 25%. The width is again much larger than expected, since the damping times are predicted to scale linearly with the size of the particle, according to the complex-frequency model presented in section 1.3 and [50]. The larger width is most probably caused by local differences in elastic coupling between the particles and the medium. The average damping time is found to be in between calculated values for a sphere homogeneously surrounded by BK7 and by PVA (see Table 1.2 on page 30), but very close to the estimated value for PVA. That suggests that the PVA film is dominant for the damping, even though this film only partly surrounds the particle.

The same experiment was carried out for particles spincoated on a fused silica substrate, again in a layer of PVA (data not shown). No significant differences in the distributions of parameters as compared to the BK7 data have been observed. Since the acoustic impedances are almost identical for BK7 and fused silica [50], not much difference is expected.

We have plotted the detected electronic and vibrational responses from Fig. 5.8 against each other in scatter plots in Fig. 5.10, to visualize how the parameters are correlated. There is a strong correlation between the electronic and oscillation amplitude (Fig. 5.10A), since both parameters directly scale with the strength of the plasmon. The period and the damping time, between which a linear correlation is expected [50], show only very little correlation (Fig. 5.10B). The correlation between the oscillation amplitude and the period is also very weak (Fig. 5.10C), which means that the oscillation amplitude and

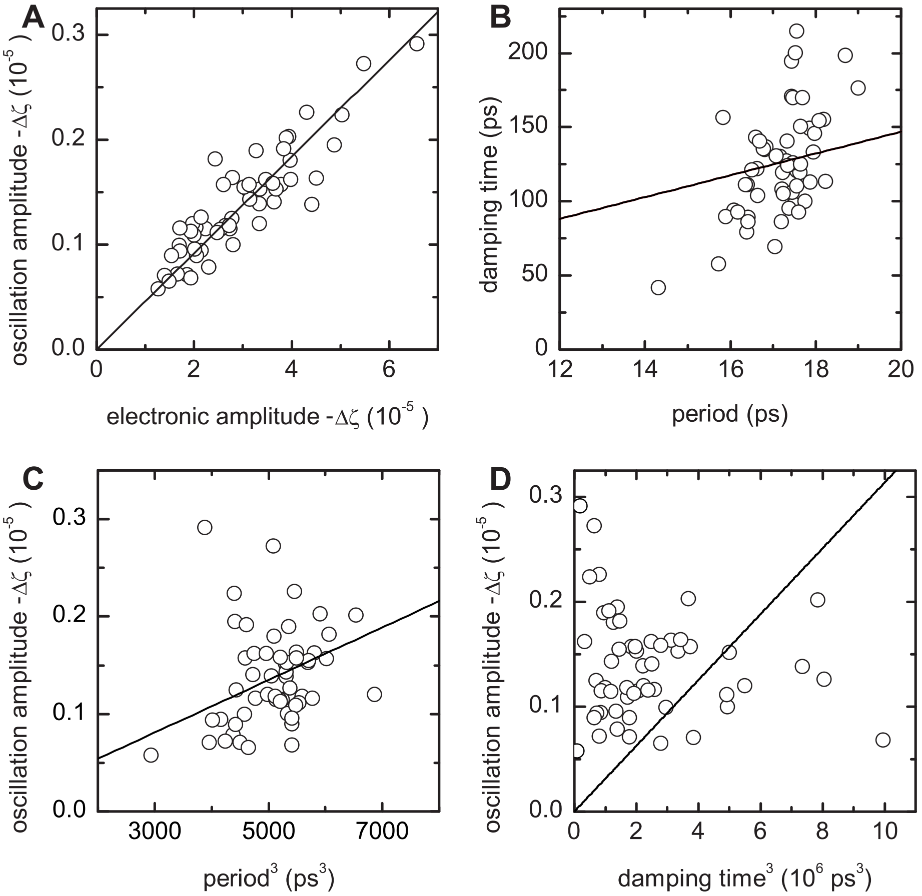

Figure 5.10: Correlation of the electronic and vibrational properties of single gold nanoparticles. The solid lines are linear fits through the origin, the open circles are the data points that were plotted in histograms in Fig. 5.8. (A) The electronic and oscillation amplitudes show a very strong correlation. (B) The period and damping time are expected to scale linearly. The correlation is weak. (C) The oscillation amplitude is expected to scale with the volume of the particle, so we should find a linear dependence of the oscillation amplitude on the third power of the period. This correlation is very weak. (D) The correlation between the oscillation amplitude and the damping time is completely absent.

the damping time are, within this size distribution, only weakly influenced by particle size. Between the oscillation amplitude and the damping time (Fig. 5.10D), there is no correlation at all.

A conclusion that can be drawn from the correlations and the widths of the histograms, is that both the surface plasmon resonance and the damping time are highly influenced by the local environment. For the electronic and oscillation amplitudes as well as for the damping time, there is hardly any size dependence observed within the particle distribution. The vibration period on the other hand, is hardly affected by the local environment. The distribution of detected periods can be fully explained from the size distribution of the sample.

A sample from the same batch was coated with a layer of silica by Peter Zijlstra and James Chon (Swinburne University Melbourne), using a method by LizMarzan et al. [9, 109]. A TEM image in which the coating is clearly visible is shown in Fig. 5.9A. Since aggregation of the particles in a PVA solution was feared, they were spincoated without PVA on fused silica glass. Delay traces were measured for 87 particles, and the corresponding histograms are shown in Fig. 5.11. The distribution of electronic amplitudes in Fig. 5.11A is not monomodal. Two peaks appear, both can be fitted with Gaussian distributions and the center of the second peak is twice as high as the center of the first peak. Very likely, double particles cause the second peak. These particles are not so close together that their plasmons influence each other, which would lead to a red shift of the absorption spectrum as observed in Fig. 5.2C, but close enough to fall in the focal volume together. The reason for observing pairs is not completely clear. It might be that the silica coating favors aggregation, it could be caused by the fact that the substrates were not cleaned with KOH and acetone before spincoating (as the BK7 substrates were), or it could be caused by the absence of PVA, which may increase the probability of agregation during spincoating. We have also observed pair formation for uncoated particles, spincoated in PVA on (uncleaned) fused silica samples, so likely, the substrate-cleaning procedure was responsible for the pair formation.

We have made a separation between single and double particles by introducing a threshold for the electronic amplitude. All particles with an amplitude above $\Delta\zeta = 3 \times 10^{-5}$ (absolute value) are classified as pairs. Obviously, in this way we will classify some single particles as doubles and vice versa, since the distributions overlap, so we have chosen the threshold as low as possible, at least to minimize the occurrence of double particles in the single-particle distribution. Figures. 5.11B, C and D, show the result of the separa-

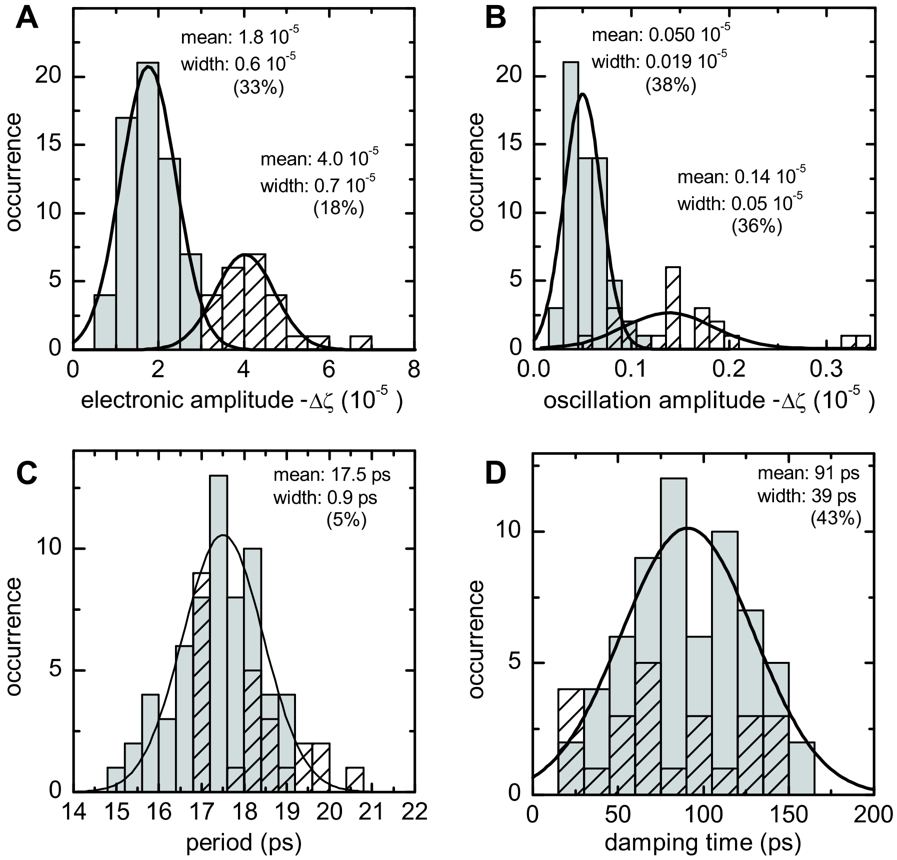

Figure 5.11: Histograms of fitted parameters of delay traces of silica-coated particles. Of 87 particles, delay traces were measured under the same experimental conditions. Shown here are the electronic amplitude (A), and the oscillation amplitude (B), period (C) and damping time (D). The particles were spincoated on a substrate of fused silica, without PVA. In contrast to the uncoated particles on BK7 glass, the electronic amplitude clearly shows two distributions. Most probably, a part of the distribution contains double particles. We have separated the single particles (grey bars) from the double particles (striped bars) using a threshold for the electronic amplitude.

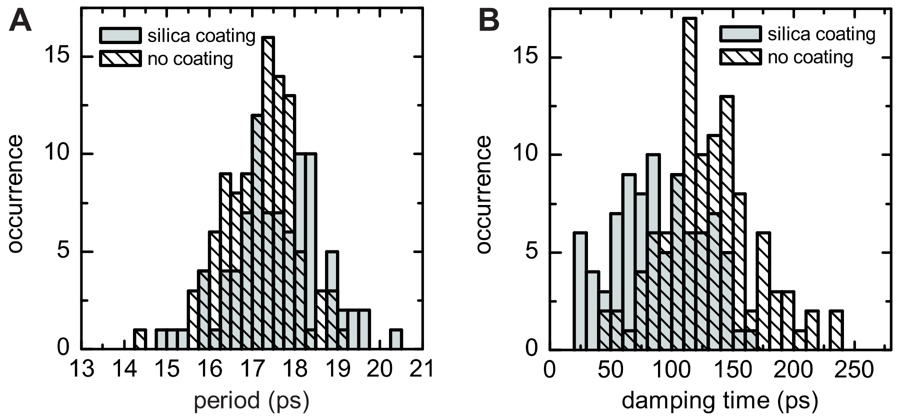

Figure 5.12: Comparison of detected period (A) and damping time (B) for large numbers of coated and uncoated gold nanoparticles. For both histograms, the number of particles is approximately 100. The uncoated particles were measured in a layer of PVA on BK7 or SiO_2 glass. The coated particles were measured without PVA on a SiO_2 substrate. The thickness of the layer was approximately 30 nm.

tion for the oscillation amplitude, period and damping time. Also for the oscillation amplitude, two distributions can be distinguished, and the particles that were classified as pairs are also here mainly in the brightest distribution. For the vibration period and the damping time, there is no clear difference between the single and the double particles, although in the distribution of the vibration period, there seems to be a small bias towards longer periods, which may be partly due to a wrong classification of large single particles as double particles.

In comparison with the uncoated particles, the coated particles damp much faster. The mean damping time is 90 ps for the selected single particles, with a width of 43%. Including the pairs did not change the mean damping time, but did increase the width of the distribution slightly, to 50%. The mean period of the selected single distribution is 17.5 ps, with a width of 5%. Here the selection seemed to be slightly biased towards smaller particles and indeed, if we include the double particles, the mean period increases slightly, to 17.6 ps, still with a width of 5%.

In order to compare the vibrational properties of coated and uncoated particles, we have plotted distributions of the vibration period and damping time of coated and uncoated particles together in Fig. 5.12. We have included the particles that were classified as doubles earlier in these distributions, since belonging to a pair does not influence the period and there was no evidence for dephasing from comparing the damping times of single and double particles, and we have also included the uncoated particles on a fused silica substrate. The Gaussian fits of Figs. 5.8C and 5.11C returned periods of 17.3 ps for uncoated particles and 17.6 ps for coated particles, and also a statistical calculation of the average periods yielded a slight difference: 17.2 ± 0.1 ps for the uncoated particles and 17.6 ± 0.1 ps for the uncoated particles, the error here is the standard error of the mean. The damping times show a larger difference. The Gaussian fits returned values of 126 ps for the uncoated particles and 86 ps for the coated particles, with widths of 26% and 48% respectively. A statistical calculation resulted in mean values of 130 ± 4 ps and 89 ± 4 ps, with standard deviations of 29% and 41%. It has to be noted that in the experiments with uncoated particles, the particles were partly embedded in a layer of PVA, which was absent in the experiments with coated particles. Though the vibration period is not very sensitive for the environment of the particle, the damping time is very much so, which means that the comparison is not completely correct. That said, the presence of PVA decreases the damping time, since the impedance mismatch with gold is larger for air than for PVA. Therefore, the observed difference in damping time would only be larger if the two experiments would have been done in the same matrix.

The change in vibration period can be explained from the added mass of the silica shell. Sader et al. have modelled the vibrations of core-shell particles [110], and predict a decrease in frequency to 85% of the frequency of an uncoated particle, taking the bulk values of the density and sound velocities of SiO_2. We see a much smaller shift, to 97%. This may well be caused by a difference in density and sound velocity of our shell, which is thin and porous, with an air content of 10-20%, compared to bulk values.

The average damping time that we find for the coated particles is close to the calculated value for a sphere embedded in a SiO_2 matrix. The differences may be explained by the fact that our shell is thin and porous. This could first of all lead to deviations from the bulk values for the density and the sound velocities of SiO_2. Secondly, the complex-frequency model assumes that the environment extends to infinity, which it clearly does not in the experiment. This will most probably also lead to deviations in the calculated values.

To summarize this section, we have conducted a statistical analysis of electronic and vibrational properties of single gold nanoparticles. It was shown that both the plasmon resonance and the vibrational damping time were strongly dependant on the local environment, which is promising for applying gold nanoparticles as local probes of acoustic and optical properties of materials. Time-resolved experiments on single gold nanoparticles coated with a layer of silica revealed an influence of the coating on the vibrational periods and damping times of the particles.

5.4 A closer look at ellipsoidal deformation

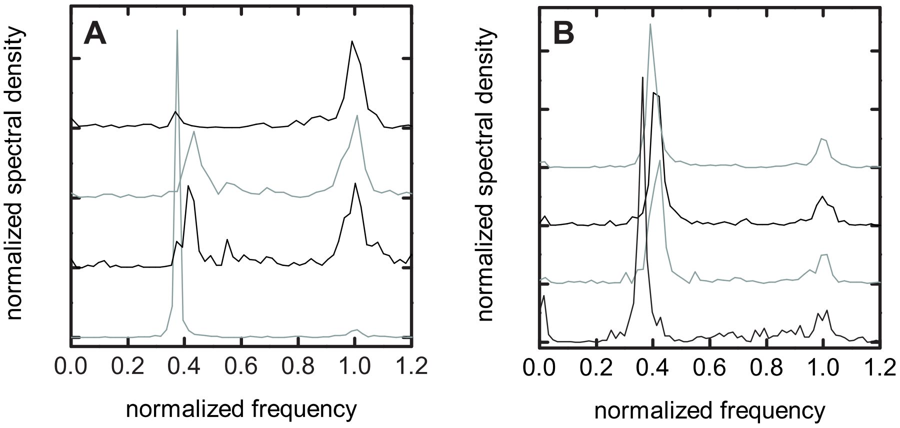

Figure 5.13: Examples of Fourier spectra of gold nanoparticles for which ellipsoidal deformation is observed. For all particles, the frequency was normalized to the frequency of the breathing mode, using a fit to a Lorentzian. Uncoated particles (A) and silica-coated particles (B) did not show a significant difference in the ratio between the breathing mode and the ellipsoidal mode. For both configurations a small variation in this ratio, between 0.37 and 0.42, has been detected. The resolution of the traces is 1 GHz. The spectral density of all traces has been normalized to the spectral density of the breathing mode, except for the bottom trace in (A) which has been normalized to 0.1× the spectral density of the breathing mode. The spectra are offset for clarity.

In this section we discuss more detailed measurements on particles that undergo ellipsoidal deformation, which was shown for the first time in section 4.5. The main question we try to answer is why we see this signal only for a rare number of particles, and if we see it, why it is so strong. In section 4.5, we discussed the necessity of a broken symmetry to launch the ellipsoidal mode, and we suggested that the glass substrate was responsible for this symmetry breaking. By correlating white-light spectra to vibrational properties and by examining the influence of the probe wavelength on the ellipsoidal mode, here we try to test this hypothesis. The experimental method was similar to that of the previous section. Unless otherwise mentioned, all measurements in this section were done with a probe wavelength of 590 nm.

The acoustic spectra shown in this section were obtained from Fourier transforms of measured delay traces.

Figure 5.13 shows examples of Fourier spectra for particles that undergo an ellipsoidal deformation, for uncoated particles as well as for particles coated with a layer of silica. For all spectra, the frequency axis was normalized to the frequency of the breathing mode. We do not see a difference in the frequency ratio between the ellipsoidal mode and the breathing mode for uncoated (Fig. 5.13A) and coated (Fig. 5.13B) particles. We did however for both samples observe a slight variation between the particles, the ratio ranging between 0.37 and 0.43. Also, it appears for some of the particles that the breathing mode is split. Some care needs to be taken in claiming the observation of split lines, since the magnitude of the splitting is comparable to the noise level. We have however in some cases observed multiple measurements of split lines in which the dip appeared always at the same frequency.

We have correlated FFT spectra to white-light scattering spectra (Fig. 5.14) for particles that showed ellipsoidal information. The white-light spectra were measured using the method explained in section 5.2.1. These experiments were done on the air-glass interface, where the background from reflection from the interface is much higher than on a nearly index-matched interface of glass and immersion oil, as was used in section 5.2. As a result, the Xenon lamp was not powerful enough as a light source and we used a tapered fiber generating a supercontinuum white light (NT&C, Stuttgart) in-

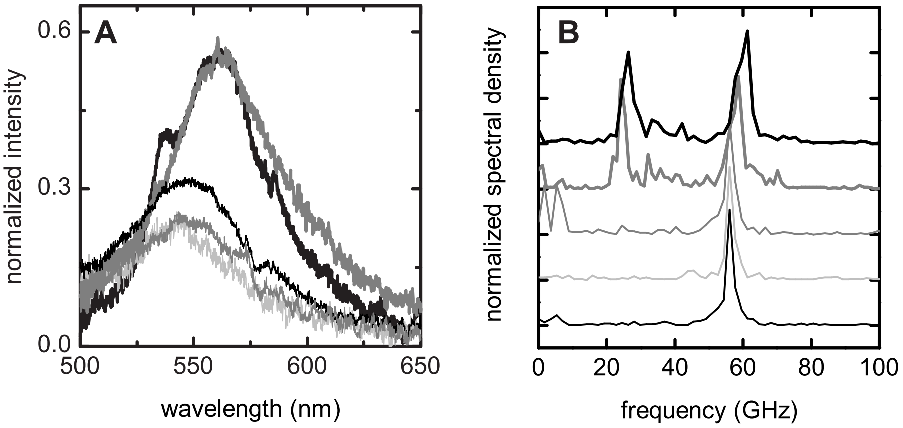

Figure 5.14: Correlation between white-light spectra (A) and Fourier spectra (B) for particles that show ellipsoidal deformation. Each different color represents a different particle and the color coding is the same for both (A) and (B). The spectra are offset for clarity and normalized to the spectral density of the breathing mode.

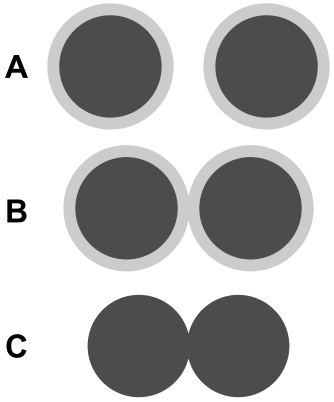

Figure 5.15: Sketch of the possible configurations for close pairs of nanoparticles. In (A) and (B), the particles are surrounded by a thin organic capping layer, whose thickness is estimated to be in the order of 1 nm. In (A), the particles are well separated, and there is no interaction. In (B), the capping layers touch, but there is no electronic contact between the particles. In (C) a touching conformation without capping layer is sketched. In this configuration, the electrons are delocalized over the two particles.

stead. Slight fluctuations in power and spectral shape of this source in combination with the small signal-to-noise ratio made it difficult to record stable spectra. Fig. 5.14A shows spectra of five different particles. The corresponding spectra are plotted in Fig. 5.14B, where the color coding is the same as in A. Although the spectra show some random fluctuations, the spectra of particles that show ellipsoidal deformation (thick lines) are remarkably different from the others (thin lines); the peak intensity is higher and the spectra are significantly red shifted.

These results point towards a different origin of the ellipsoidal deformation than the explanation that was suggested earlier. We find strong evidence that it is not the glass surface but a second particle, in mechanical contact, that is the cause of the symmetry breaking. It is important to clarify the various configurations for a pair of particles that are in close proximity. A sketch of the possibilities is given in Fig. 5.15. To stabilize the particles in solution, and to prevent aggregation, our particles are surrounded by an organic capping layer, with a thickness in the order of 1 nm. This capping layer is drawn in light grey in the figure. Two particles can be close enough to fall in the same focal volume, but too far from each other to have any mutual influence (Fig. 5.15A). This configuration was seen in Fig. 5.11. If their distance decreases, the particles come close enough for their plasmons to polarize each other (Fig. 5.15B). This will create a longitudinal plasmon, an additional red-shifted mode in the spectrum. In the configuration sketched in Fig. 5.15B, the particles are in mechanical contact, since the capping layers touch, but electronic contact (i.e. delocalization of the electrons over the two particles) is prevented by the capping layer. In Fig. 5.15C, a configuration is drawn in which the capping layer is removed (e.g. by an intense laser beam or an electron beam). In this case, the electrons are delocalized over both particles, creating a single system with the shape of a dumbbell. This will lead to a dramatic red shift of the longitudinal mode and a large change in the vibrational properties of the particles. In a recent study, Danckwerts and Novotny [111] have calculated scattering spectra for two gold nanoparticles as a function of their mutual distance. They found that upon approach, there is a gradual red shift of the spectrum, but as soon as the particles touch electronically, the spectrum undergoes a sudden red shift towards near-infrared wavelengths.

Our experimental observations agree with the conformation in Fig. 5.15B as the origin of the strong ellipsoidal mode. The organic layer prevents electronic contact between the particles, but can act as a spring to transfer mechanical energy, launching the ellipsoidal deformation of the particles. First of all, the splitting of the line of the breathing mode (see Fig. 5.13), as well as the strong electronic amplitude for particles with ellipsoidal deformation (which can be three to four times above the average signal), suggest that more than one particle is present in the focal volume. Secondly, the red-shifted plasmon suggests that we see a mode associated with a longitudinal deformation. If we compare the spectra with those of Ref. [111], we see that the two spectra drawn with thick lines in Fig. 5.14 are consistent with an inter-particle distance in the order of 1 nm, but not with a configuration with electronic contact. Also, the ratio between the breathing mode and the ellipsoidal mode that we detect is consistent with that of a sphere (see Table 1.1 on page 27), which implies that we detect vibrations of spheres and not of dumbbell systems. Although it is difficult to calculate the vibrational frequencies for a dumbbell system as in Fig. 5.15C (the frequencies will depend largely on the contact area), surely the ratio between the breathing mode and the ellipsoidal mode will be different for a dumbbell than for a sphere.

If the ellipsoidal mode is indeed connected to a longitudinal plasmon, we would expect this mode to become stronger if the probe wavelength is longer. Figure 5.16 shows an experiment in which the delay traces of 3 particles were measured at three different probe wavelengths: 570 nm, 590 nm, and 625 nm. The Fourier spectra were then normalized to the spectral density of the ellipsoidal mode, which was determined with a fit to a Lorentzian line shape.

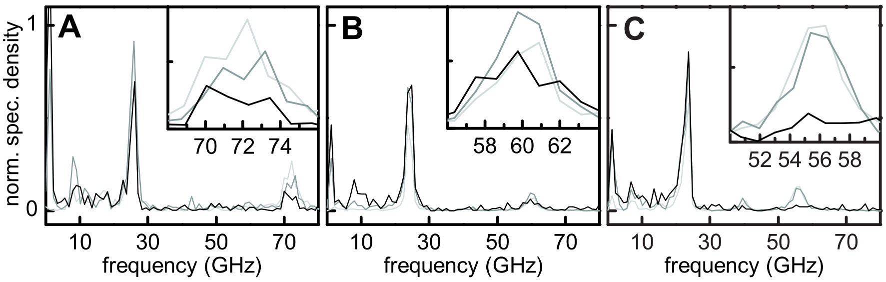

Figure 5.16: Wavelength dependence of the relative intensity of the ellipsoidal mode. Three different particles are shown in panels (A), (B) and (C) respectively. Each particle was measured with three different probe wavelengths, 570 nm (light grey in B and C), 575 nm (light grey in A), 590 nm (dark grey) and 625 nm (black). The spectra were then normalized to the intensity of the ellipsoidal mode, using a fit to a Lorentzian. The insets show an enlargement of the lines of the breathing mode. Note that a third peak appears at 40 GHz for the third particle.

For two of the three particles, the relative intensity of the breathing mode is lower for a longer pump wavelength. This strongly suggests a link between the longitudinal plasmon and the ellipsoidal-deformation mode.

As a final remark, we state that the fact alone that we detect the ellipsoidal mode for coated particles, rules out the glass surface as a source of the symmetry breaking. In TEM images of many coated particles, we did not find any uncoated particles, so all particles were embedded in a relatively homogeneous environment. We did find several occurrences of two particles within a single coating.

The final question that remains is whether we can detect the ellipsoidal mode for particles of which we are sure that they are single. The answer to that question is shown in Fig. 5.17, where we have added all the Fourier transforms of the traces of the uncoated particles of which the statistical analysis was shown in Fig. 5.8, after their frequencies were normalized to the frequency of their breathing mode. In Fig. 5.17A, where this was done for the particles spincoated on BK7 glass, a peak rises out of the background at a frequency of approximately 0.4 times the frequency of the breathing mode, exactly where we find the ellipsoidal mode. Although we cannot exclude the possibility that this peak is caused by noise, this could mean that there is a very weak trace of the ellipsoidal mode present in the single particles as well, one that could not be detected in the individual contributions. Note that if this peak is indeed noise, we can at least define it as the upper limit for the strength of the ellipsoidal mode for single particles. For particles spincoated

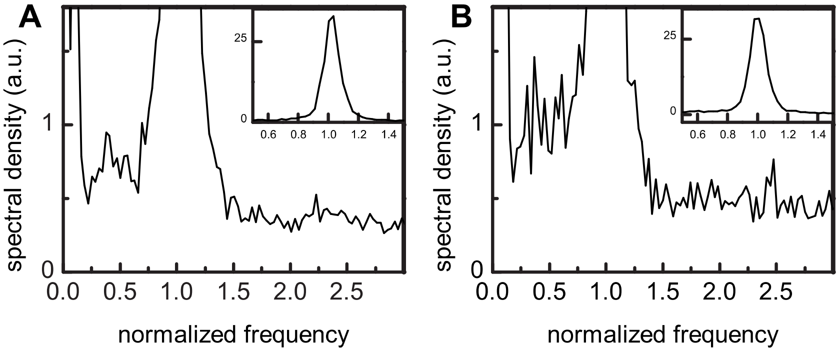

Figure 5.17: Summation of frequency-normalized Fourier spectra of single gold nanoparticles on BK7 glass (A) and fused silica glass (B). Fourier spectra of around 50 delay traces of particles spincoated in PVA on either BK7 glass or fused silica glass were fitted to a Lorentzian. The frequency axis was then normalized to the frequency of the breathing mode that was returned by the fit, before all traces were added. In (A), a peak can be seen rising out of the background at a normalized frequency of 0.4. Note that in both (A) and (B), it appears as if there is a very weak signal rising above the background at normalized frequencies between 2 and 2.5. If this is indeed a signal, it is probably a trace of the $(n, l) = (1, 0)$ mode.

on SiO_2 (Fig. 5.17B), there is an increase in the spectral density below the breathing mode, but no clear peak can be distinguished. This implies a huge amplification of the ellipsoidal mode by the second particle. The ellipsoidal mode in Fig. 5.17 is estimated to be at least 100 times smaller than the breathing mode (note that this number should be regarded as a lower limit), while the ellipsoidal mode can be equally large or even larger than the breathing mode if a second particle is present.

In conclusion, we did not find significant differences in ellipsoidal deformation between free and silica-coated particles. We found slight variations in the frequency ratio of the ellipsoidal mode and the breathing mode that may be due to splitting of the ellipsoidal mode. Most importantly, several observations all point to the proximity of a second particle, separated by the organic capping layer electronically but not mechanically, as the trigger of the ellipsoidal deformation. Electron microscopy could confirm this conclusion, since it can directly visualize two connected particles. For such measurements, care needs to be taken of the order in which the electron microscopy and pump-probe experiments are executed, since the electron beam will burn the protective capping layer away from the particles, thereby completely changing their behavior.

5.5 Conclusion

In this chapter, several experiments in which optical properties are correlated with the structure of individual particles have been presented. Using white light scattering, we could combine pump-probe experiments with a measurement of the absorption spectrum. This confirmed theories and earlier experiments on the origin of the detected phenomena, but unfortunately, a quantitative comparison of calculations with the experiment was not possible. Statistical analysis of large numbers of single-particle pump-probe parameters gave promising results for the utilization of the acoustic vibrations of single gold particles as local probes of acoustic parameters of a medium. Finally, several experiments on particles that showed ellipsoidal deformation could identify mechanical coupling of two nanoparticles as the origin of the strong amplitude of the ellipsoidal modes.

Nevertheless, the experiments are still hampered by uncertainties, caused by inhomogeneous environments and uncertainties about the shape of the particles. Also, possible deviations of the acoustic parameters of gold on the nano scale might lead to unexpected results. Eventually, we expect that experiments in more homogeneous media and correlation of pump-probe experiments with electron microscopy on the same particle, can lift these uncertainties one by one.